9

Research Article

Xiaohui Du, Chenyue Liu, Zefei Ding, Yuan Zhao, Cunguang Zhu, Yaoyao Wang* and Pengpeng Wang*

High-repetition-rate ultrafast fiber lasers enabled by BtzBiI₄: a novel bismuth-based perovskite nonlinear optical material

https://doi.org/10.1515/nanoph-2025-0087 Received February 20, 2025; accepted May 18, 2025; published online June 30, 2025

Abstract: Recent advances in perovskite crystals have highlighted their exceptional optical properties, making them promising candidates for a wide range of photonic applications. However, the exploration of high-repetition-rate laser systems based on these materials remains underdeveloped, hindering their potential in ultrafast laser technologies and related fields such as optical communications and precision metrology. In this study, we present, for the first time, the saturable absorption characteristics of a novel organic-inorganic hybrid perovskite incorporating the heavy metal bismuth (Bi), specifically NmethylbenzothiazoleBiI4 (BtzBiI4). The material was integrated as a saturable absorber (SA) into a passively mode-locking erbium-doped fiber laser. By harnessing the exceptional optical nonlinearity of BtzBiI₄-SA, we successfully achieved stable fundamental mode-locking, harmonic mode-locking, and bound-state soliton mode-locking within a single cavity. The fundamental mode-locking yielded pulses with a duration of 844 fs and a signal-to-noise ratio of 66.15 dB. Additionally, the 142nd-order harmonic solitons attained an impressive repetition rate of 1.3202 GHz. These results represent a significant step forward in the realization of high-repetition-rate fiber lasers utilizing perovskite materials. Our findings highlight the remarkable potential of BtzBiI_4 as a high-performance nonlinear optical material, paving the way for next-generation ultrafast photonic devices.

Keywords: perovskite crystals; saturable absorber; ultrafast fiber lasers; mode-locking; harmonic mode-locking

1 Introduction

High-repetition-rate (HRR) mode-locked fiber lasers have garnered significant attention due to their exceptional performance across diverse fields. For instance, as light sources for optical frequency combs and optical communication systems, HRR fiber lasers can significantly enhance data transmission rates and improve signal integrity [1], [2]. In nanomanufacturing, HRR fiber lasers deliver highenergy-density pulses, enabling precise material processing with minimal thermal damage [3]. Furthermore, in medical imaging and laser surgery, HRR fiber lasers facilitate high-resolution imaging and accurate tissue ablation [4]. To realize HRR pulse fiber lasers, various methods have been explored, including cavity length reduction, the incorporation of comb filters such as Fabry-Perot and micro ring filters, and harmonic mode-locking (HML) techniques, encompassing both active and passive HML [5]. While cavity length plays a crucial role in determining laser repetition rates, its further reduction is constrained by the gain fiber length, rendering it an unsustainable strategy for achieving higher repetition rates [6]. The integration of comb filters alongside highly nonlinear photonic devices within the laser cavity enables HRR generation through dissipative four-wave mixing mode-locking. However, this method is limited by complex fabrication processes for precision filters and significant insertion losses [7]. Active HML achieves high-frequency pulse outputs exceeding 10 GHz,

Liaocheng University, Liaocheng, China,

E-mail: wangyaoyao@lcu.edu.cn (Y. Wang),

wangpengpeng@lcu.edu.cn (P. Wang).

https://orcid.org/0000-0001-7562-6938 (Y. Wang).

https://orcid.org/0000-0002-0307-8837 (P. Wang)

Xiaohui Du, Chenyue Liu, Zefei Ding, Yuan Zhao and Cunguang Zhu, Liaocheng University, Liaocheng, China,

E-mail: dd15169505459@163.com (X. Du), 13969147875@163.com (C. Liu), 19863936682@163.com (Z. Ding), 13345185784@163.com (Y. Zhao), cunguang_zhu@163.com (C. Zhu).

https://orcid.org/0009-0007-2705-9538 (X. Du).

https://orcid.org/0009-0002-0323-9482 (C. Liu).

https://orcid.org/0009-0001-6006-0983 (Z. Ding).

https://orcid.org/0009-0006-4900-3044 (Y. Zhao).

https://orcid.org/0000-0003-2343-7689 (C. Zhu)

^{*}Corresponding authors: Yaoyao Wang and Pengpeng Wang,

but it is restricted by the slow temporal response of external modulators, leading to relatively broad pulse widths [8]. Conversely, passive HML is regarded as a more favorable approach for achieving HRR, as it represents a specific multipulse operation regime in which pulse peak power is constrained by the soliton area theorem [9]. According to the soliton area theorem, pulse energy is influenced by both dispersion and nonlinear parameters within the laser cavity. In the fundamental mode-locking state, a stable balance between dispersive and nonlinear effects maintains pulse integrity. As pump power increases, this balance progressively deteriorates; when dispersion becomes insufficient to counteract enhanced nonlinearity, the increased pulse energy triggers pulse splitting. Stronger nonlinear effects accelerate this splitting process, leading to an increase in repetition rates and ultimately achieving HRR operation. Eventually, the pulses restabilize due to the combined contributions of dispersion and nonlinearity [10]. In the HML regime, pulses originating from the fundamental mode-locking state undergo splitting and arrange uniformly as pump power increases and polarization states are finely adjusted. The repetition rate of pulses in the HML state is an integer multiple of that in the fundamental mode-locking state, underscoring the role of highly nonlinear photonic devices in enabling HRR generation [11]. Significant advancements in this field have been demonstrated using various saturable absorbers (SAs). In 2012, Grzegorz et al. reported the use of graphene as an SA in an erbium-doped fiber laser (EDFL), achieving a maximum repetition rate of 2.22 GHz (21st-order harmonic) [12]. In 2013, Luo et al. employed a microfiber-based topological insulator Bi₂Te₃ in a fiber laser, realizing HML at 2.04 GHz (418th-order harmonic) [13]. Similarly, in 2014, Liu et al. demonstrated mode-locked pulses at 2.5 GHz (369th-order harmonic) using a microfiber-based MoS2-SA in an EDFL [14]. More recently, in 2020, Huang et al. utilized MXene (V₂CT_x) as an SA, successfully achieving 206th-order HML at 1.01 GHz [15]. In 2022, Lee et al. utilized V2AlC-based saturable SAs to achieve mode-locked pulses at a repetition rate of 1.3 GHz, corresponding to the 86th-order harmonic, in an EDFL [16]. In the same year, Kong et al. reported the pioneering application of ZnO/Co₃O₄ nanocomposites as SAs in EDFLs, generating high-order HML pulses with repetition rates of 1.465 GHz (242nd-order harmonic) and 1.114 GHz (181th-order harmonic) [17]. These studies illustrate the immense potential of advanced materials, including carbon nanotubes, graphene, topological insulators, transition metal dichalcogenides (TMDs), and MXenes, for achieving HRR in ultrafast fiber lasers. These materials exhibit excellent nonlinear optical properties but also face several

challenges. For example, graphene, due to its zero bandgap and low optical absorption efficiency, limits its application in high-power lasers [18], [19]. TMDs, although showing tunable bandgap properties and excellent nonlinear absorption performance, typically exhibit direct bandgap characteristics only in their monolayer form, which requires complex synthesis processes [20], [21]. The topological insulator Bi₂Se₃, while possessing remarkable topological effects, suffers from low thermal conductivity and optical damage threshold, restricting its stability in high-power laser applications [22]-[24]. Although MXene materials exhibit high nonlinear optical responses and ultrafast carrier mobility, their susceptibility to oxidation limits their long-term stability in practical applications [25], [26]. Thus, the search for novel saturable absorber materials, particularly those with enhanced stability, environmental adaptability, and superior nonlinear absorption performance, has become a crucial direction in laser technology research [27]-[31]. In this context, we propose a new type of SA – BtzBiI₄, a bismuth-based organic-inorganic hybrid perovskite with a narrow bandgap of 1.94 eV and a significant nonlinear optical response [32]. Compared to existing materials, BtzBiI₄ not only exhibits excellent optical absorption properties but also demonstrates improved stability and resistance to oxidation, making it a promising candidate for applications in ultrafast lasers.

Recently, perovskite crystalline materials have demonstrated tremendous potential across diverse high-tech fields due to their exceptional optoelectronic properties and multifunctionality [33], [34]. In photovoltaics, perovskite solar cells have rapidly emerged as formidable alternatives to traditional silicon-based solar cells, owing to their high light absorption coefficients, tunable bandgaps, cost-effective solution processing, and remarkable power conversion efficiencies. Over the past decade, the power conversion efficiencies of perovskite solar cells have increased from an initial 3.8 % to over 25 %, nearing the efficiency limits of single-crystal silicon solar cells [35], [36]. Moreover, the flexibility and transparency of perovskite materials unlock new possibilities for next-generation wearable electronics and building-integrated photovoltaic systems [37], [38]. In lightemitting applications, perovskite light-emitting diodes have gained significant traction in display technologies and lighting devices due to their high color purity, broad color gamut, and exceptional brightness. By engineering the composition and structure of perovskite materials, efficient light emission spanning the ultraviolet to near-infrared regions can be achieved, underscoring their promise for full-color displays and solid-state lighting [39]. Additionally, perovskite materials have exhibited impressive performance in lasers,

photodetectors, memory devices, and sensors. Perovskitebased lasers, featuring low lasing thresholds and high gain coefficients, are particularly promising for biomedical imaging and optical communication [40]. Similarly, perovskite photodetectors, renowned for their high sensitivity and broad spectral response, are widely utilized in environmental monitoring and advanced imaging technologies [41]. Furthermore, perovskite-based memories and sensors leverage their excellent electrical and ionic migration properties, offering innovative solutions for high-density data storage and ultra-sensitive detection systems [42], [43]. Collectively, these findings highlight the immense potential of perovskite crystalline materials for applications in photovoltaics, light emission, optoelectronic detection, and storage sensing. Continued advancements in material science and fabrication techniques will undoubtedly further expand the practical utility and performance of perovskitebased devices [44]-[47].

In this study, we successfully synthesized lead-free perovskite crystals (BtzBiI₄) and systematically characterized their morphology, crystal structure, and optical properties. Based on these investigations, the nonlinear optical properties of BtzBiI4 nanomaterials were thoroughly explored. A sandwich-structured SA incorporating BtzBil₄ nanomaterials was fabricated via a direct coupling method, and its nonlinear absorption behavior at 1.5 µm was evaluated. The carrier dynamics of the material were examined using femtosecond transient absorption spectroscopy, while its nonlinear absorption parameters were further assessed through a balanced twin-detector setup. The fabricated SA demonstrated a modulation depth of 8.51 % and a saturation intensity of 47.19 MW/cm², indicating excellent saturable absorption performance. Additionally, open-aperture Z-scan measurements revealed a third-order nonlinear optical coefficient of 1.03×10^{-11} m/W for BtzBiI₄. Incorporating the BtzBiI₄-SA into an EDFL cavity enabled the successful realization of stable fundamental mode-locking, high-order HML, and bound-state modelocking. Specifically, the fundamental mode-locking operation exhibited a repetition rate of 9.294 MHz, a central wavelength of 1,560.388 nm, a 3-dB bandwidth of 3.24 nm, and a pulse duration of 844 fs. Furthermore, the 142nd-order harmonic mode-locking achieved an ultrahigh repetition rate of 1.3202 GHz. The observed bound-state solitons featured a center wavelength of 1,560.04 nm with a pulse separation of 4.073 ps. These results convincingly demonstrate the potential of BtzBiI₄ as an efficient SA for HRR fiber lasers, paving the way for future developments in ultrafast photonic technologies.

2 Synthesis and characterization

2.1 Preparation of BtzBiI₄

This research investigates lead-free, bismuth-based perovskite crystals containing ionic liquids, which were successfully synthesized through an in situ method. The preparation process, illustrated in Figure 1, involved adding 0.2 mL of benzothiazole to a mixed solution of 3.0 mL acetonitrile and 2.0 mL methanol. The mixture was stirred for 10 min, followed by the addition of 1.0 mL hydriodic acid and 0.589 g BiI₃. After stirring for 30 min, the resulting red transparent solution was subjected to ultrasonic treatment for 4 h. The solution was then transferred to a 15 mL stainless steel autoclave and heated at 140 °C for 72 h. Gradual cooling to room temperature allowed for the slow formation of high-quality crystals (C₈H₈NSBiI₄, CCDC: 2388135). Upon completion, the product, isolated as a single crystalline phase with an 81 % yield (based on the bismuth content), exhibited distinct red massive crystals and was designated as BtzBiI₄.

2.2 Characterization of BtzBiI₄

The morphology, crystal structure, optical absorption, and scattering properties of the synthesized BtzBiI₄ crystals were characterized prior to use. After coating the sample with gold for 1 min using an ion sputtering apparatus (GVC-2000, Oxford Quorum), the morphology and particle size distribution of the BtzBiI₄ dispersion were examined using a scanning electron microscope (SEM, Zeiss Sigma 300). Figure 2a(I) –(III) show images at scales of 2 μ m, 1 μ m, and 500 nm, respectively. The dispersed material exhibited an irregular block-like morphology (Figure 2(a)) with clear layered structures visible in Figure 2a(I) and (II). Transmission electron microscopy (TEM, FEI Tecnai F20) was used to analyze the crystal distribution at micro- and nanoscale levels. Figure 2b(I)-(III) show images at scales of 1 μm, 200 nm, and 10 nm, respectively. The BtzBiI₄ samples displayed uniform lattice arrangements with consistent distribution. A selected lattice fringe in Figure 2b(III) reveals a calculated lattice spacing of 0.217 nm, indicating high crystallinity and structural stability of BtzBiI₄. Elemental distribution was analyzed using energy-dispersive spectroscopy (EDX, Oxford Xplore 30), and the EDX mapping results are shown in Figure 2(j). The analysis indicated a mass ratio of Bi to I of approximately 2:5, consistent with the molecular formula. Figure 2(c) presents the elemental mapping, where yellow, purple, red, blue, and green represent I, Bi, C, S, and

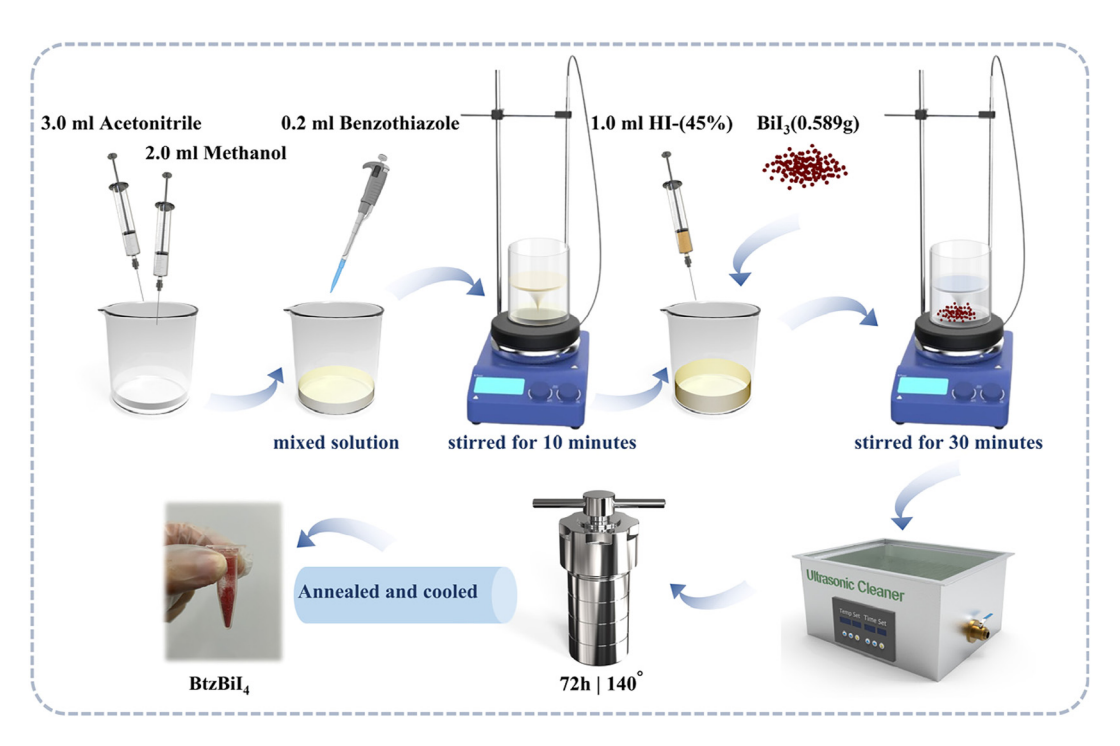


Figure 1: Schematic illustration for the preparation of BtzBiI₄ crystals.

N, respectively, confirming the uniform distribution without agglomeration. Single-crystal X-ray diffraction (SCXRD) analysis reveals that the BtzBiI₄ molecular structure consists of two primary components: a discrete M⁺ cation (with M corresponding to Btz in BtzBiI₄) and a one-dimensional, continuous anionic chain of $(BiI_4)^-$ (Figure 2(d) and (e)). Within the unit cell of BtzBiI₄ (Figure 2(f)), eight (Btz)⁺ cations are symmetrically arranged along the four sides of the unit cell, whereas the (Bi₂I₁₀)⁴⁻ anionic fragments are located at the base-centered positions.

To precisely determine the thickness of the BtzBiI₄ nanosheets employed in the sandwich-structured SA, atomic force microscopy (AFM) analysis was carried out using a Bruker Dimension ICON system. As presented in Figure 2(g), the AFM image reveals that the nanosheets exhibit a uniform and smooth surface morphology, indicative of high-quality material preparation. The corresponding height profile shown in Figure 2(h) confirms that the nanosheets possess a thickness ranging from approximately 3–5 nm. This ultrathin configuration significantly enhances the light-matter interaction at the nanoscale, thereby contributing to efficient nonlinear optical modulation, which is crucial for the realization of high-performance ultrafast photonic devices. The crystal structure of BtzBiI₄ was examined via X-ray diffraction (XRD) using a Bruker D8 Advance system. As depicted in Figure 2(i), the blue and red lines represent the simulated and experimental values, respectively. The experimental diffraction spectrum exhibits pronounced

peaks at $2\theta = 8.18^{\circ}$, 9.34° , 13.67° , 27.46° , and 41.66° , which align precisely with the simulated diffraction peaks. To further investigate the molecular structure of BtzBiI₄, Raman spectroscopy (Horiba Scientific Labram HR Evolution) was employed, and the Raman scattering spectra are shown in Figure 2(k). Three characteristic Raman vibrational modes were identified at 101.54 cm⁻¹, 134.55 cm⁻¹, and 269.14 cm⁻¹, corresponding to the Bi-I bonding structure within the (BiI₄) unit. These results are consistent with those reported for (BAH)BiI₄ crystals in previous studies [48]. To elucidate the absorption properties of BtzBiI₄ nanosheets, Ultraviolet-Visible-Near Infrared (UV-VIS-NIR) optical spectra were measured using a UV-3600-Plus spectrophotometer (Shimadzu). The absorption spectra, as shown in Figure 2(1), exhibit broadband absorption in the 1,500-1,600 nm range. Overall, these characterization results demonstrate that BtzBiI₄ possesses remarkable crystallinity, uniform particle size distribution, and absorption capability at 1.5 µm, thereby ensuring its reliability and stability for optoelectronic device applications.

3 Nonlinear optical response

3.1 Fabrication of BtzBiI₄-SA

A sandwich-structured BtzBiI₄-SA was successfully fabricated using a direct coupling technique, and its nonlinear saturable absorption properties were systematically

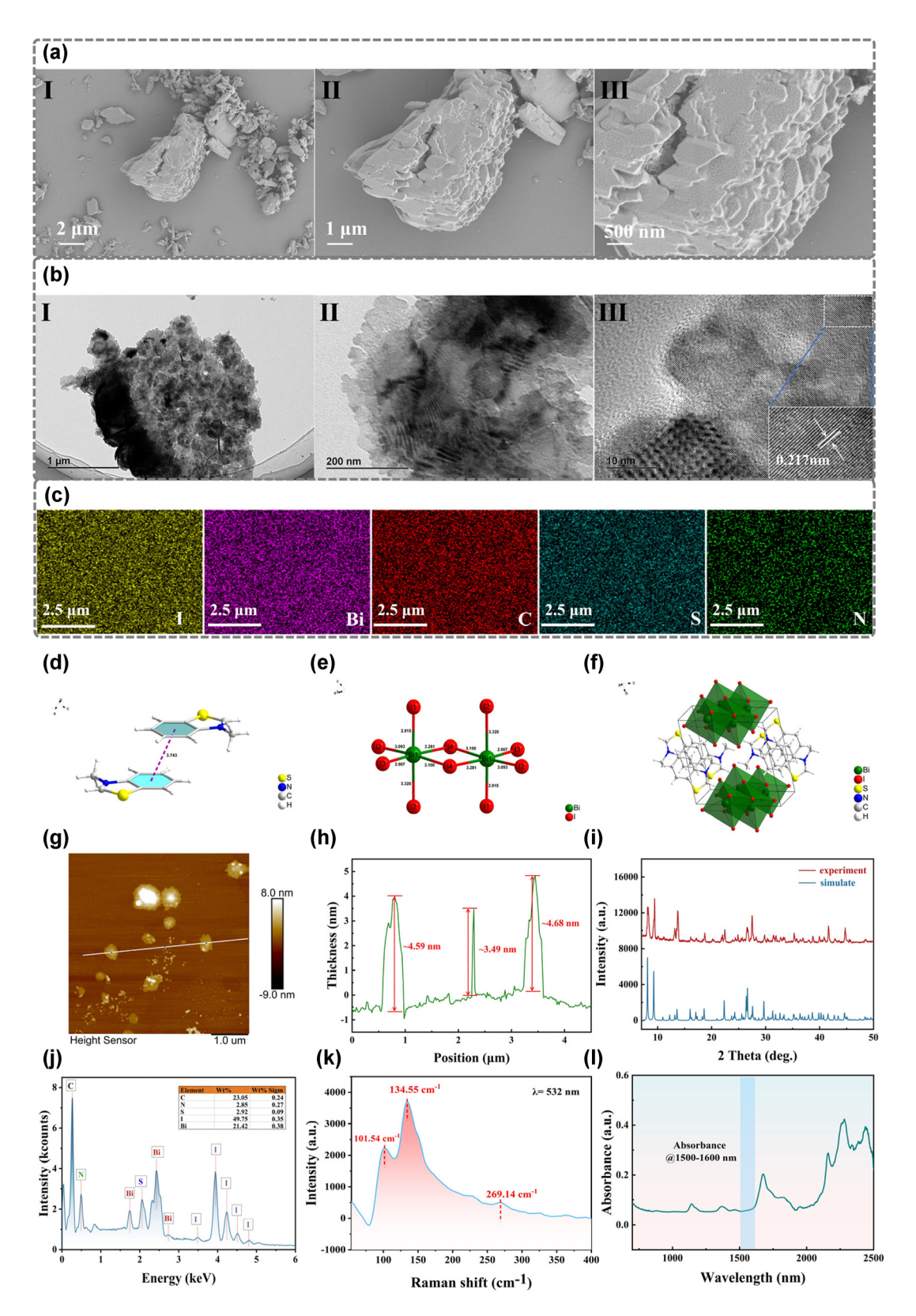


Figure 2: Characterization of BtzBiI₄. (a) SEM images of BtzBiI₄, (b) TEM images of BtzBiI₄, (c) mapping images of BtzBiI₄, (d) view of the centroid-to $centroid \ \pi \cdots \pi \ interaction \ between two \ adjacent \ Btz^+ \ countercations, (e) \ the \ edge \ shared \ BiI_6 \ octahedral \ in \ BtzBiI_4, (f) \ side \ view \ of \ single \ unit \ cell$ of BtzBiI₄ along the *a* direction, (g) AFM image of BtzBiI₄ nanosheets, (h) height profile extracted from the AFM image, illustrating the thickness characteristics, (i) XRD pattern of BtzBiI₄ powder, (j) EDX spectrum of BtzBiI₄ powder, (k) Raman spectrum of BtzBiI₄ powder, and (l) UV-VIS-NIR spectrum of BtzBiI₄ powder.

characterized. To prepare the device, 10 mg of the synthesized BtzBiI₄ crystals were placed in a glass petri dish for selection. Using an optical microscope (DVE3630, Otter Optics), a crystal with a relatively regular morphology and a diameter of approximately 125 µm was identified. The selected crystal was then carefully transferred onto the end face of an optical fiber using a fiber probe. Under microscopic observation, it was confirmed that the crystal completely covered the fiber core, ensuring effective coupling. Finally, two optical fiber jumpers and a flange were assembled to create the sandwich structure, thereby completing the fabrication of the BtzBiI₄-SA (Figure 3(a)).

3.2 Saturable absorption of BtzBiI₄-SA

Examining the nonlinear optical response, underlying mechanisms, and the interaction of light with nanostructures provides a broader context for understanding the unique characteristics of BtzBiI₄-SA. Recent studies on the nonlinear behavior of quantum dot materials and the interaction of light with nanostructures offer valuable comparisons to our work. For instance, Yu et al. [49] investigated the nonlinear optical response of lead telluride quantum dots in all-solid-state pulse lasers, while Zhu et al. [50] developed MXene V₂CT_v nanosheet/bismuth quantum dot heterostructures, enhancing nonlinear optical properties. Additionally, Finke et al. [51] explored temperature-resistant quantum dot saturable absorbers for integration into semiconductor lasers. Other studies, including those on Ag₂S quantum dots [52] and phosphorene quantum dots [53], focus on their applications in biosensing and optoelectronic detection [54], [55]. Building on these insights, the nonlinear optical response of BtzBiI₄-SA was systematically investigated using a balanced twin-detector configuration, as shown in Figure 3(b). This approach provides a detailed understanding of the material's nonlinear characteristics, essential for its potential in ultrafast photonic applications. The experimental apparatus comprises a high-power seed laser, a tunable variable optical attenuator (pVOA-1550-1-B-30-SM-B, Max-ray Photonics), and an optical coupler (OC). The seed laser, a custom-built erbium-doped fiber laser employing nonlinear polarization rotation (NPR) for mode-locking, generates pulses at a central wavelength of 1,562.32 nm, with a pulse width of 788 fs and a repetition frequency of 25.12 MHz. The NPR fiber laser system integrates a 976 nm laser diode (Model: PUMPL-976-1550-FA-B-YP), two polarization controllers (PCs), and a polarization-dependent isolator (PD-ISO) to sustain stable NPR mode-locking. Additional components include erbium-doped fiber (EDF), single-mode fiber (SMF-28), a wavelength division multiplexer (WDM),

and an optical coupler. In this configuration, 20 % of the laser output is guided through the tunable attenuator and subsequently divided into two channels by a 50:50 optical coupler. One path is directly injected into a power meter, while the other path passes through the BtzBiI₄-SA before being directed into the same power meter. By adjusting the parameters of the optical attenuator, the output power of the NPR fiber laser can be modulated. A nonlinear transmission curve was derived from the measured data and subsequently fitted using a standard saturable absorption model (Eq. (1)).

$$T(I) = 1 - \Delta T \exp(-I/I_{\text{sat}}) - T_{\text{ns}} \tag{1}$$

In the nonlinear absorption model, T(I) represents the transmittance, ΔT is the modulation depth, I is the incident light intensity, $I_{\rm sat}$ is the saturation intensity, and $T_{\rm ns}$ denotes the nonsaturable losses. The measurement results are shown in Figure 3(c), indicating that as the incident light power increases, the absorption of BtzBiI₄-SA gradually decreases and eventually reaches saturation. The ΔT is 8.51 %, the $I_{\rm sat}$ is 47.19 MW/cm², and the $T_{\rm ns}$ is 60.09 %. These results demonstrate that BtzBiI₄-SA exhibits excellent nonlinear saturable absorption properties, making it a promising SA for passive mode-locking fiber lasers. Compared with conventional SAs (Table S1, see Supplementary Material), BtzBiI₄ exhibits a MD of 8.51 %, which is competitive with materials such as NbTe2 and BP. Notably, BtzBiI4 demonstrates an exceptionally high I_{sat} of 47.19 MW/cm², surpassing many reported materials (e.g., MXene-film and MXene-DS), and thus shows great potential for high-power ultrafast laser applications. A high $I_{\rm sat}$ typically indicates strong tolerance to intense laser irradiation, although it may also imply an elevated damage threshold. For ultra-highpower lasers, appropriate protective measures are recommended to ensure material stability and prevent damage under prolonged high-intensity exposure. Overall, BtzBiI₄ presents significant advantages as a saturable absorber, especially for high-power and HRR lasers. Nevertheless, for certain extreme operating conditions, it is crucial to balance the high saturation intensity with the material's damage threshold to ensure long-term operational reliability.

The saturable absorption properties of 2D materials are fundamental to their role as absorbers in pulsed laser systems. At low light intensities, these materials exhibit linear absorption. However, as the incident optical power increases, their absorption behavior becomes nonlinear. As the intensity rises, the absorption decreases, and the transmission increases, which is characteristic of the saturable absorption effect in 2D materials [56]. To probe the nonlinear absorption characteristics of BtzBiI₄, the

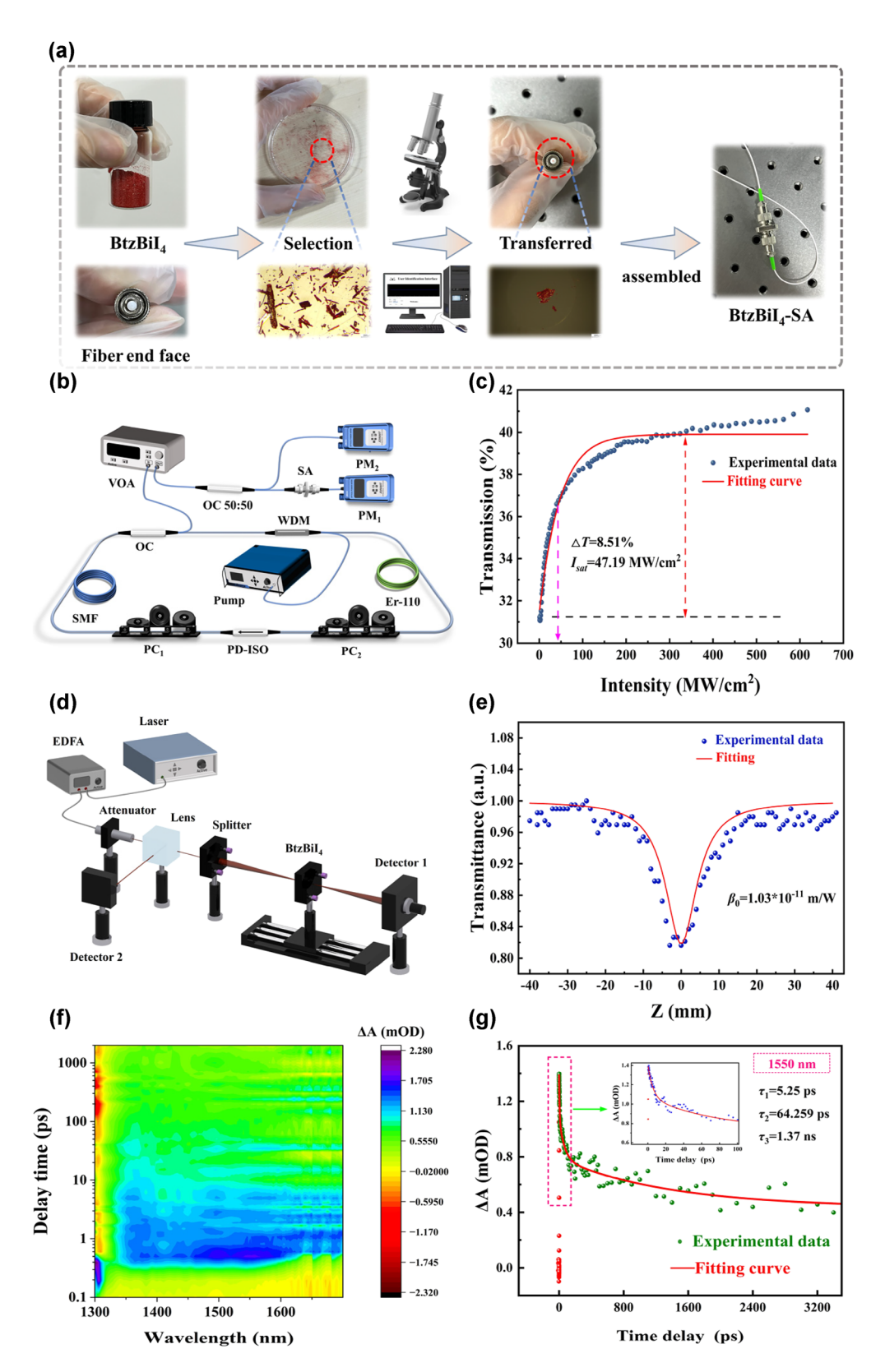


Figure 3: Characterization of BtzBiI₄. (a) Preparation of BtzBiI4-SA. (b) Schematic of the balanced twin-detector technique. (c) Saturable absorption characteristics of BtzBiI4-SA. (d) Schematic diagram of open-aperture Z-scan system. (e) Z-scan curves of BtzBiI4 nanomaterials. (f) The 2D transient absorption color-coded map of BtzBiI4 material. (g) Dynamic curves at 1,550 nm of BtzBiI4 nanomaterials.

open-aperture Z-scan technique, based on spatial beam distortion, was employed for the measurements. As illustrated in Figure 3(d), a custom-built NPR mode-locking fiber laser, amplified by an erbium-doped fiber amplifier (EDFA-PA35-B), was used as the light source for the Z-scan system. The optical beam was collimated using a fiber collimator (GCX-L30APC-1550) and subsequently split by a 10:90 beam splitter (GCC-403234). Ninety percent of the beam was directed through a focusing lens with a focal length of 50.8 mm (GCL-M010109N) and a quartz plate (φ 25 mm × 2 mm, infrared, JGS3) coated with BtzBiI₄ material, and then detected by a thermopile detector (GCI-080202). The power was recorded using an optical power meter (GCI-08). The remaining 10 % of the beam was directly detected by a second thermopile detector as a reference. During the experiment, the power values were varied by continuously adjusting the position of the quartz plate along a sliding track. The Z-axis zero point was positioned at the focal point of the lens, with the propagation direction of the beam aligned along the positive Z-axis. As the sample moved along the positive Z-axis, the intensity of the incident light varied due to the self-focusing or self-defocusing effects occurring within the sample. By comparing the data recorded by detector 1 and detector 2, the nonlinear absorption properties of the sample were obtained. The normalized transmittance T(z) was calculated using the following formula (Eq. (2)):

$$T(z) = 1 - \beta_0 \cdot L_{\text{eff}} \cdot I_0 / \left[2\sqrt{2} \left(1 + z^2 / z_0^2 \right) \right]$$
 (2)

where T is the normalized transmittance, z represents the relative position of the sample along the Z-axis with respect to the lens focal point, $L_{
m eff}$ denotes the effective length of the material, z_0 is the Rayleigh length, and β_0 and I_0 correspond to the nonlinear absorption coefficient and the peak axial intensity at the focal point (z = 0), respectively. As shown in Figure 3(e), the β_0 was determined to be 1.03×10^{-11} m/W through curve fitting. Nonlinear absorption typically results from a combination of SA, reverse saturable absorption, and two-photon absorption. While reverse saturable absorption and two-photon absorption contribute to enhanced optical absorption, saturable absorption leads to an increased irradiance threshold for effective absorption in the material. This interplay of mechanisms defines the material's nonlinear optical behavior and its potential applications in ultrafast photonic devices.

3.3 Transient absorption characteristics of the as-prepared BtzBiI₄ nanomaterials

To explore the ultrafast carrier dynamics of BtzBiI₄ in greater detail, femtosecond time-resolved transient absorption (TA) spectroscopy was applied to investigate the carrier relaxation pathways (Figure S1; see Supplementary Material). An 1,150 nm pump laser was utilized to promote electrons from the ground state to the excited state, while a broadband white light source spanning 1,300-1,700 nm functioned as the probe beam. The delay time, representing the temporal difference between the pump and probe pulses, was employed to monitor the evolution of the carrier dynamics. The TA modulation signals ($\Delta A = A_1 - A_0$) were derived by measuring the absorption levels in the presence (A_1) and absence (A_0) of pump excitation, providing insights into the absorption behavior under high and low excitation conditions. As illustrated in Figure 3(f), BtzBiI₄ exhibits broadband absorption near 1,550 nm, with pronounced absorption in the long-wavelength region (>1,300 nm) facilitated by electronic transitions. Figure 3(g) presents the dynamic curve at a probe wavelength of 1,550 nm, showing the evolution of ΔA with delay time. These results demonstrate a dynamic transition from photoinduced excited-state absorption to a bleaching signal. The TA curves were fitted using a three-exponential decay function (Eq. (3)):

$$\Delta A = A_1 \cdot \exp(-t/\tau_1) + A_2 \cdot \exp(-t/\tau_2)$$

$$+ A_3 \cdot \exp(-t/\tau_3) \tag{3}$$

In this context, A_1 , A_2 , and A_3 denote the amplitude components, while t represents the delay time. The parameters au_1 , au_2 , and au_3 correspond to the response times associated with distinct carrier dynamic processes. Upon pump excitation, ground-state electrons - including those localized at oxygen vacancy defects – are elevated to excited states. When subjected to probing at different wavelengths, these excited electrons absorb photon energy, facilitating their transition to higher excited states. This phenomenon manifests as photoinduced absorption peaks, which are indicated by the dashed regions in Figure 3(g). The formation of photoinduced absorption peaks is closely associated with carrier thermalization and relaxation processes [57]. The high intensity of the photoinduced absorption peaks indicates the strong photo absorption capability and high carrier density of BtzBiI₄, underscoring its excellent saturable absorption properties and significant potential for nonlinear optical applications. Moreover, the rapid picosecond-scale decay process is attributed to bulk electron-hole recombination, while the longer bleaching duration is linked to defect-state electron trapping and recombination with holes [58]–[60]. The transient absorption characteristics of BtzBiI₄ are particularly vital for mode-locking lasers. A shorter τ_1 facilitates rapid responses, enabling the generation of ultrashort pulses in mode-locking lasers. Meanwhile, intermediate τ_2 and longer au_3 contribute to stabilized mode-locking and HRR pulse outputs, making BtzBiI₄ highly suitable for applications requiring pulse-width tuning or pulse shaping.

4 Experimental setup

The schematic of the ring-cavity passively mode-locking EDFL employing the BtzBiI₄-SA is illustrated in Figure 4. The system is pumped by a 976 nm laser diode (LD PUMPL-976-1550-FA-B-YP), with light coupled into the ring cavity through an integrated optical module that includes a 976/1,550 nm WDM, a polarization-independent isolator (PI-ISO), and a 10/90 OC. The PI-ISO enforces unidirectional light propagation within the cavity, preventing potential damage from back reflections. The OC directs 10 % of the intracavity power as output, with the remaining 90 % recycled to sustain oscillation. A PC fine-tunes the polarization state and adjusts cavity birefringence. The gain medium, a 32-cm EDF (Er-110 Nufern SM-ESF-4/125), exhibits a dispersion of -46 ps/nm/km at 1,550 nm. Nonlinear phase shifts are accumulated through 12 m of SMF (G652D SMF-28, Corning) with a dispersion of 17 ps/nm/km at 1,550 nm. Accounting for the pigtail lengths of all components, the total cavity length measures 22.11 m, corresponding to a net dispersion of -0.4534 ps^2 . The BtzBiI₄-SA, serving as the modelocking element, demonstrates excellent saturable absorption properties by transmitting high-intensity components of the stimulated emission while attenuating weaker ones. This iterative process enables the formation of a stable single pulse after thousands of cavity round trips. For pulse characterization, the system includes a spectrum analyzer (AQ6370D, Yokogawa), a digital oscilloscope (MDO3102, Tektronix), a radio frequency spectrum analyzer (FPC1000, Rohde & Schwarz), an autocorrelator (PulseCheck 50, APE), a 3 GHz photodetector (PD-03-FA-D, Max-ray Photonics), and an optical power meter (JW3208C, Joinwit).

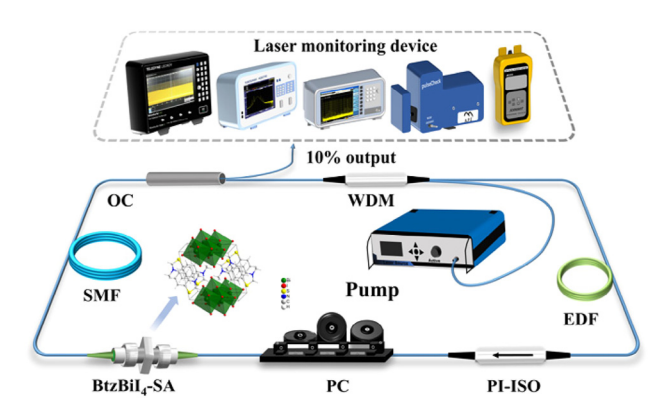


Figure 4: Schematic of the erbium-doped fiber laser.

5 Results and discussion

5.1 Fundamental mode locking

When the coupled pump power was increased to 97 mW, mode-locking was initiated, leading to the generation of multiple pulses within the cavity. By adjusting the polarization state, a pulse train with a repetition rate of 9.294 MHz was achieved. Under the fundamental mode-locking state, the laser's performance was evaluated at an output power of 365 mW, as recorded in Figure 5. To begin with, the mode-locking spectrum reveals a central wavelength of 1,560.388 nm, accompanied by a 3 dB spectral bandwidth of 3.24 nm (Figure 5(a)). Notably, the presence of distinct Kelly sidebands in the spectrum confirms that the laser operates within the conventional soliton regime, signifying soliton-like behavior. Furthermore, the pulse train shown in Figure 5(b) exhibits uniformly spaced pulses, which clearly indicate stable mode-locking operation. The pulse interval, measured as 107.6 ns, corresponds precisely to the cavity length of 22.11 m, thereby validating the experimental setup's precision. In addition, a detailed view of a 5 µs pulse sequence highlights consistent spacing and stable intensity, further emphasizing the reliability and temporal stability of the mode-locking mechanism. Moving on to the pulse duration, the autocorrelation trace fitted with a sech² function reveals a duration of 844 fs (Figure 5(c)). The calculated time-bandwidth product (TBP) is 0.3529, close to the Fourier transform limitation (0.315) for sech²-shaped pulses, suggesting the presence of slightly chirped pulses. To further assess the laser's operational stability, the radio frequency (RF) spectrum was analyzed (Figure 5(d)). The measured signal-to-noise ratio (SNR) of 66.15 dB underscores the high stability of the BtzBiI₄-SA-based laser system. Additionally, the pulse spectrum recorded over a 1 GHz span confirms uniformly distributed pulses, providing further evidence of excellent stability and pulse quality (Figure 5(e)). As the pump power increased from 164 mW to 472 mW, both the average output power and single-pulse energy exhibited a linear growth trend. The average output power rose from 2.97 mW to 10.92 mW, while the corresponding singlepulse energy increased from 0.319 nJ to 1.175 nJ (Figure 5(f)). This linear relationship suggests efficient energy conversion in the laser cavity, reflecting the stability and scalability of the mode-locking performance under varying pump powers. The optical spectra at various power levels, the 12-h pulse train at fixed pump power, and the 12-h output power stability test indicate that the fabricated SA maintains long-term stable operation under high irradiance without degradation, ensuring consistent and

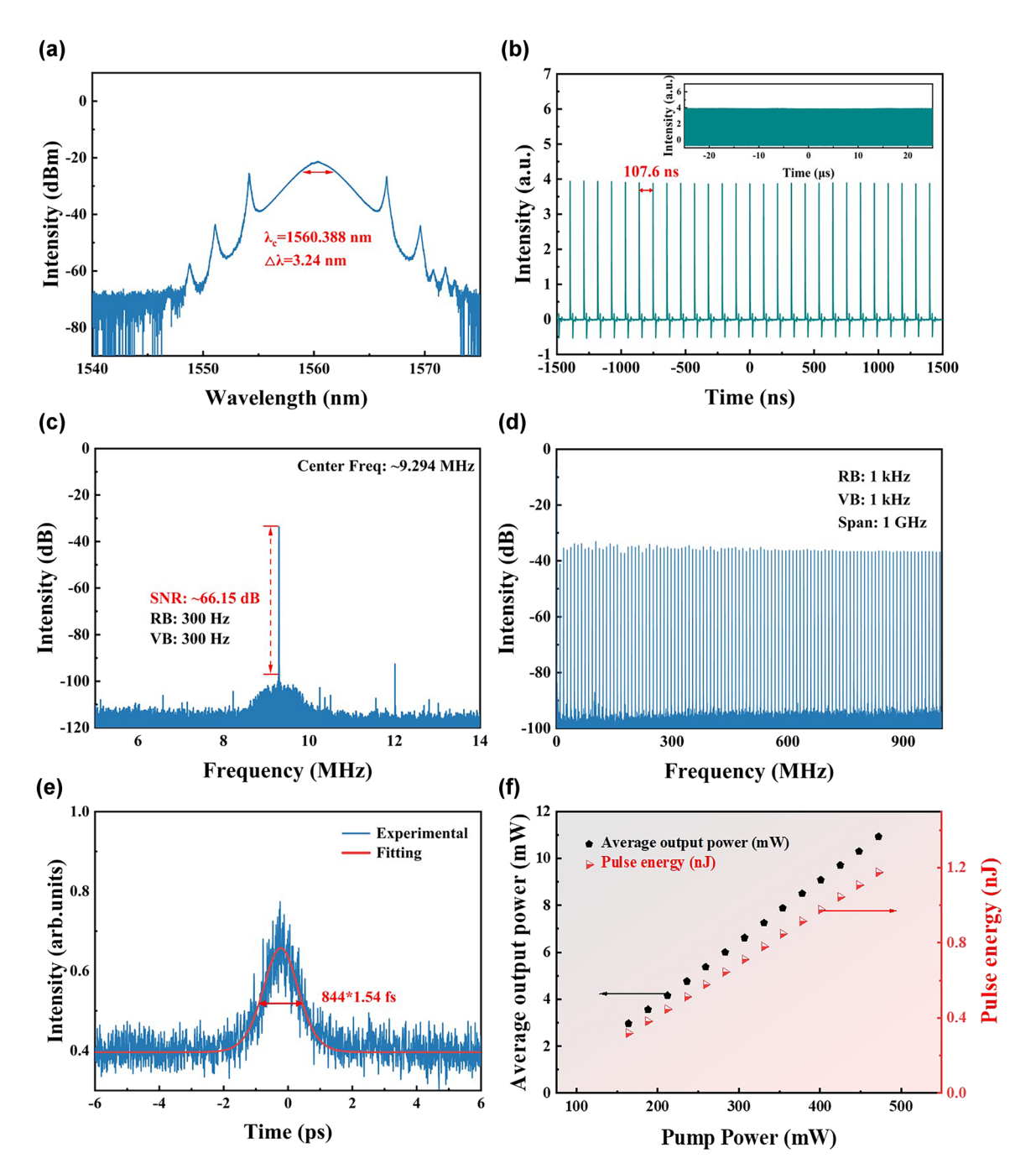


Figure 5: Characteristics of fundamental mode locking. (a) Optical spectrum. (b) Oscilloscope trace. (c) RF spectrum. (d) RF spectrum within the 1 GHz range. (e) Autocorrelation trace. (f) Spectral variations at different pump powers.

high-quality laser output (Figure S2a-c; see Supplementary Material).

5.2 Harmonic mode locking

By carefully tuning the PC and progressively increasing the pump power, HML pulses with varying repetition rates were successfully generated. During the transition to higher harmonic orders, transient instabilities in the pulse train were observed, which subsequently stabilized into new harmonic states as a result of intracavity nonlinear effects and gain competition. At a pump power of 391 mW, the pulse characteristics under the 28th, 41st, 55th, 65th, 70th, 76th, 92nd, and 106th HML conditions are presented in Figure 6. As shown in Figure 6(a), the pulse trains of different harmonic orders exhibit uniform

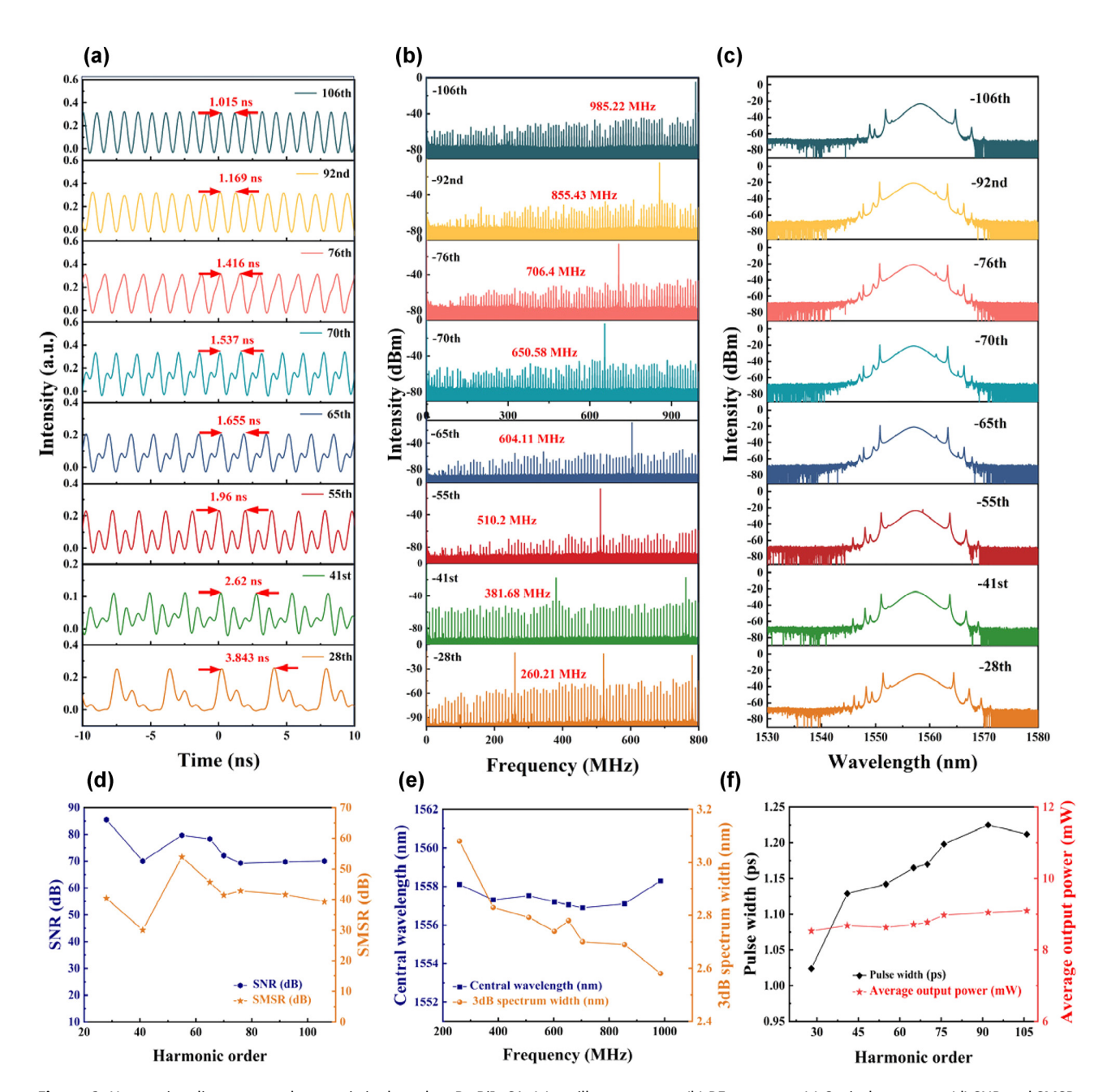


Figure 6: Harmonic soliton output characteristics based on BtzBiI₄-SA: (a) oscilloscope trace. (b) RF spectrum. (c) Optical spectrum. (d) SNR and SMSR of harmonic mode-locking pulses. (e) Central wavelength and 3 dB bandwidth variation with repetition frequency. (f) Pulse width and average output power variation with harmonic order.

and stable distributions. The measured peak time intervals were 3.843 ns, 2.62 ns, 1.96 ns, 1.655 ns, 1.537 ns, 1.416 ns, 1.169 ns, and 1.015 ns, respectively. These intervals directly correspond to the repetition frequencies of the harmonic pulses, demonstrating a significant decrease in pulse spacing as the harmonic order increases. The RF spectra in Figure 6(b) validate the precise repetition frequencies, measured as 260.21 MHz, 381.68 MHz, 510.2 MHz, 604.11 MHz, 650.58 MHz, 704.23 MHz, 855.43 MHz, and 985.22 MHz for the

respective harmonic orders. Furthermore, the SNRs of these pulses exceed 70 dB, indicating stable signals with minimal noise, while the side-mode suppression ratios (SMSRs), all above 30 dB, confirm excellent spectral purity and reduced mode competition (Figure 6(d)). The optical spectra of the HML pulses, depicted in Figure 6(c), exhibit typical soliton features with prominent Kelly sidebands. The central wavelength remains stable around 1,558 nm, as illustrated in Figure 6(e). However, the 3 dB spectral bandwidth

narrows from 3.08 nm to 2.58 nm as the harmonic order increases, likely due to spectral filtering effects in highorder harmonics. The relationship between harmonic order, pulse duration, and average output power is detailed in Figure 6(f). Notably, while the pulse duration broadens from 1 ps to 1.25 ps with increasing harmonic order—likely due to nonlinear effects, dispersion, and phase-matching constraints—the average output power remains nearly constant, indicating conserved energy per pulse (Figure S3a-h; see Supplementary Material).

By gradually increasing the pump power, the repetition rate exceeded 1 GHz when the pump power was adjusted to 413 mW. Further tuning of the polarization state enabled the capture of HML at the 108th, 112nd, 114th, 122nd, 126th, and 131th orders. Detailed pulse characteristics are presented in Figure 7. Figure 7(a) shows the pulse train captured by the oscilloscope, where the pulse intervals correspond to 1/108, 1/112, 1/114, 1/122, 1/126, and 1/131 of the fundamental mode-locking pulse interval. The

exact repetition frequencies were measured by a radio frequency spectrum analyzer (DSA875, RIGOL) with a resolution of 3 kHz (Figure 7(b)), yielding values of 1.005 GHz, 1.041 GHz, 1.06 GHz, 1.134 GHz, 1.17 GHz, and 1.22 GHz. In all cases, the SMSRs exceeded 30 dB, demonstrating the stability of harmonic mode-locking. The spectral profiles remained consistent across different harmonic orders. As the pump power continued to increase, enhanced nonlinear effects within the cavity led to significant suppression of the Kelly sidebands. The central wavelength stabilized around 1,556 nm, with a 3 dB bandwidth of approximately 1.6 nm (Figure 7(c)). Furthermore, autocorrelation measurements indicated pulse durations ranging from 1.49 ps to 1.75 ps, confirming high-quality pulse characteristics in the HML regime (Figure S4a-f; see Supplementary Material).

At a pump power of 472 mW, a maximum repetition rate of 1.3202 GHz was achieved, corresponding to the 142nd-order HML. Figure 8(a)-(d) present the detailed characteristics of this high-order harmonic state. As shown

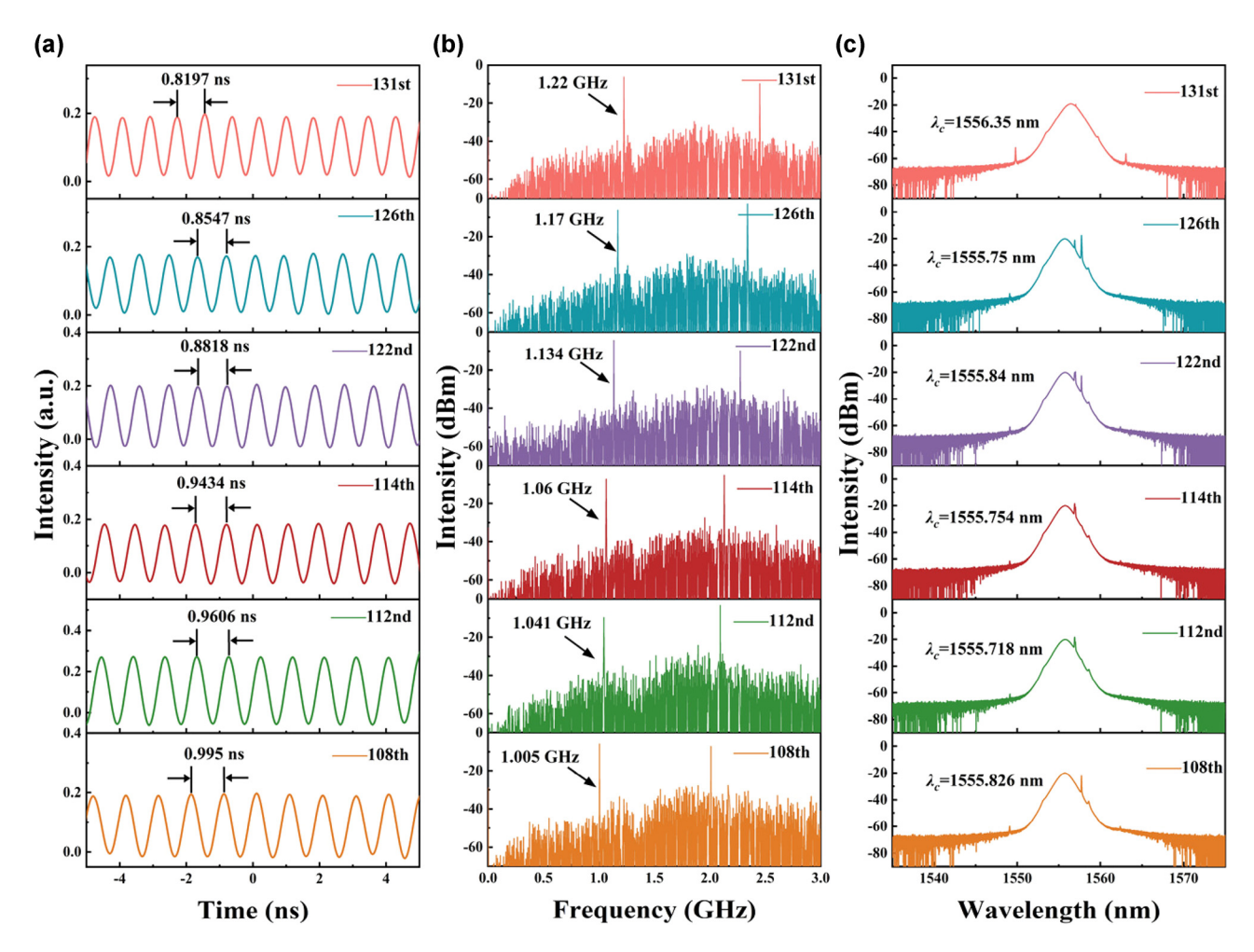


Figure 7: Harmonic soliton output characteristics based on BtzBiI₄-SA: (a) oscilloscope trace. (b) RF spectrum. (c) Optical spectrum.

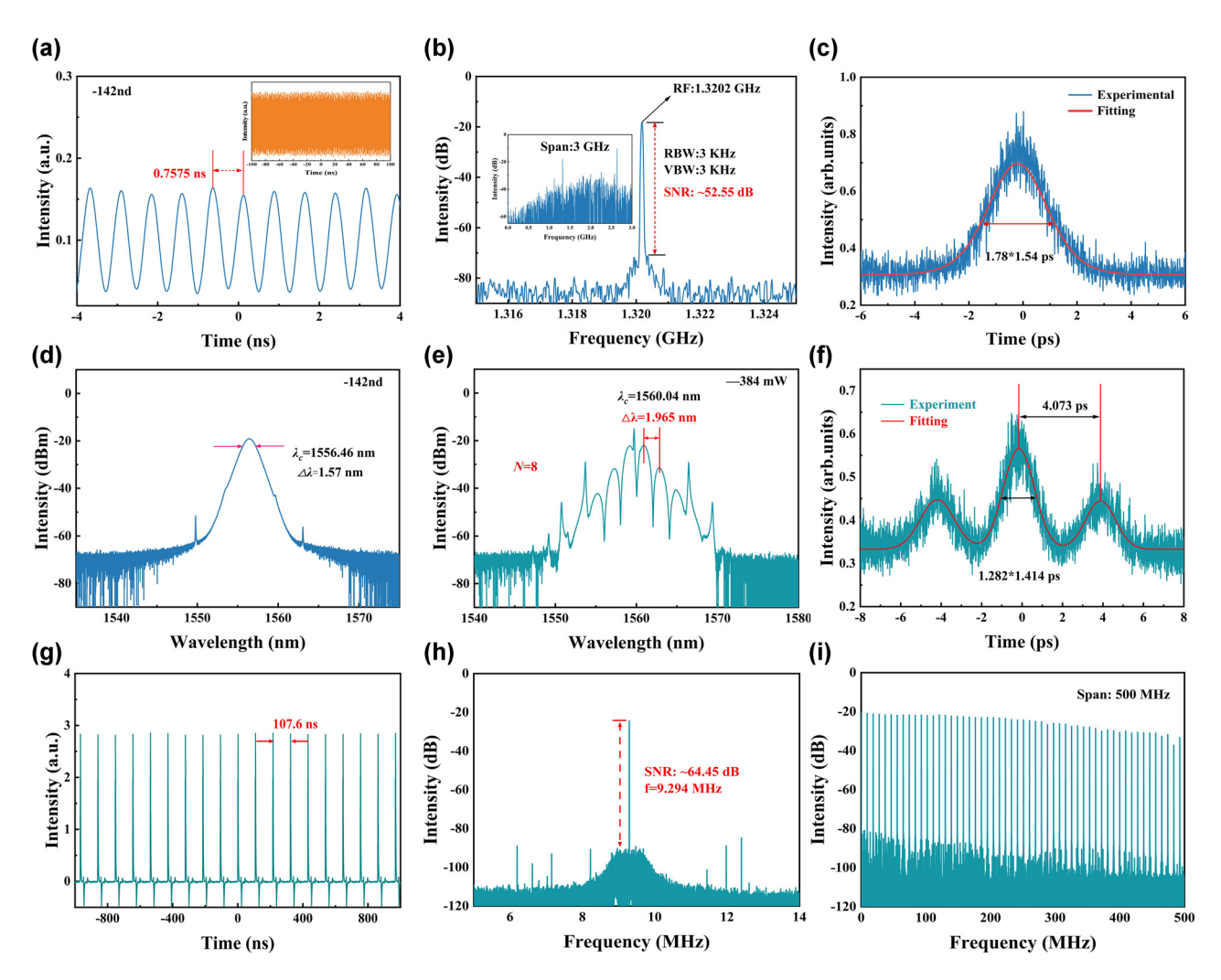


Figure 8: Characteristics of 142nd-order harmonic mode locking and bound-state solitons. (a) Pulse sequence of the 142nd-order soliton, (b) frequency spectrum of the 142nd-order soliton, (c) autocorrelation trace of the 142nd-order soliton, (d) spectrum of the 142nd-order soliton, (e) optical spectrum of bound-state solitons, (f) autocorrelation trace of bound-state solitons, (g) pulse sequence of bound-state solitons, (h) RF spectrum of bound-state solitons with a 500 MHz sweep width.

in Figure 8(a), the measured pulse interval is 0.7575 ns, precisely 1/142 of the fundamental mode-locking interval. The inset of Figure 8(a) displays a long-duration pulse train, highlighting the excellent stability of the HML operation. The RF spectrum in Figure 8(b) further confirms this stability, with the measured repetition rate of 1.3202 GHz exactly matching 142 times the fundamental frequency, thereby validating the harmonic generation. Notably, the RF spectrum exhibits a high SNR of 52.55 dB, indicative of low noise and high spectral purity. Moreover, the inset of Figure 8(b), depicting a 3 GHz span of the RF spectrum, shows no spurious peaks, providing additional evidence of stable HML operation. The autocorrelation trace in Figure 8(c), fitted with a sech² profile, yields a pulse duration of 1.78 ps. The corresponding TBP is calculated to be 0.346, suggesting slight chirping in the pulses. Spectral analysis in Figure 8(d)

reveals a central wavelength of 1,556.46 nm and a 3 dB bandwidth of 1.57 nm. This spectral narrowing aligns with typical characteristics of high-order HML and further supports the soliton-like behavior of the pulses.

5.3 Bound-state solitons

A fiber laser operates as a dynamically balanced system, highly responsive to variations in cavity parameters such as dispersion, nonlinearity, gain, and loss properties. In a laser cavity with a net negative dispersion, the interplay between self-phase modulation and group velocity dispersion creates an environment conducive to the formation of optical solitons. As the pump power continues to rise, intensified nonlinear interactions combined with peak power limitations trigger the breakup of a single soliton into mul-

Table 1: Comparison of nonlinear optical properties and performance metrics of perovskite-based saturable absorbers.

Materials	MD	Pulse repetition rate (MHz)	λ_c (nm)	Ref.
CsPbBr ₃	13.1 %	14.8	1,076	[63]
CH ₃ NH ₃ PbI ₃	8 %	4.08	1,064	[64]
CH ₃ NH ₃ PbI ₃	27.8 %	13.15	1,555	[65]
CH ₃ NH ₃ SnI ₃	15.2 %	4.03	1,064	[66]
$(C_6H_5C_2H_4NH_3)_2PbI_4$	16 %	41.8	1,565.8/1,604	[67]
(PEA) ₂ (CsPbBr ₃) _{n-1} PbBr ₄	16.5 %	17.4	1,562/1,569.5/1,558.8	[68]
Ba ₂ LaTaO ₆	24 %	12.3/550	1,557.4/1,556.6	[69]
PEA ₂ PbI ₄ NCs	20 %	29.67	1,572.68	[70]
BtzBiI ₄	8.51 %	9.294/1,320.2	1,560.388/1,556.46	This work

tiple subpulses, each exhibiting lower peak energy. These emerging pulses engage in complex interactions characterized by both repulsive and attractive forces. When these opposing forces achieve a dynamic balance, the system stabilizes, resulting in the formation of bound solitons with robust coherence [61], [62]. These are characterized by two or more pulses being bound together and moving as a group within the cavity, maintaining a constant time interval and fixed phase difference. In our study, a pair of stable bound solitons was observed when the pump power increased to 384 mW. Figure 8(e) shows the spectrum, which, in addition to the symmetric Kelly sidebands, exhibits modulation with a period of 1.965 nm. Furthermore, a significant dip at the central wavelength of 1,560.04 nm indicates that the phase difference between the bound solitons is π . The relationship between the spectral modulation period ($\Delta\lambda$) and the time-domain pulse interval ($\Delta \tau$) can be expressed using the theoretical formula (Eq. (4)):

$$\Delta \tau = \frac{\lambda_c^2}{c\Delta\lambda} \tag{4}$$

In this context, λ_c denotes the central wavelength of the bound solitons, while c represents the speed of light in a vacuum. According to this formula, the pulse interval $\Delta \tau$ is calculated to be 4.128 ps. The autocorrelation trace shown in Figure 8(f) exhibits three distinct peaks, indicating the presence of a dual-pulse bound soliton mode-locking state. The peak spacing is measured to be 4.073 ps, which corresponds well with the theoretical soliton temporal interval $\Delta \tau$. Gaussian fitting reveals that the widths of the three peaks are approximately 1.282 ps, with an intensity ratio of 1:2:1, confirming that the dual solitons exhibit identical pulse durations and intensities. The time interval between adjacent solitons is 107.6 ns, corresponding to a repetition frequency of 9.294 MHz shown in Figure 8(g). The SNR of the bound-state soliton radio frequency spectrum recorded in Figure 8(h) is 64.45 dB, demonstrating high operational stability. Additionally, the spectrum within a 500 MHz range shown in Figure 8(i) further validates the soliton's stability.

Table S2 summarizes the key performance parameters of previously reported systems alongside our work. Compared with prior studies, our laser demonstrates a significantly higher harmonic order of 142 and an ultra-high repetition rate of 1.3202 GHz, while maintaining a short pulse duration of 1.78 ps. These results confirm that our laser system not only achieves outstanding repetition performance but also preserves excellent pulse quality. Collectively, this highlights the effectiveness of the fabricated saturable absorber in enabling high-order harmonic mode-locking and its promising potential for high-speed optical communication and precision measurement applications. Building on this, Table 1 presents recent advancements in perovskitebased saturable absorbers for ultrafast lasers. Various perovskite materials have exhibited favorable nonlinear optical properties, supporting their application in modelocked laser systems. For example, CsPbBr₃ and CH₃NH₃PbI₃ have demonstrated notable modulation depths and operational performance at near-infrared wavelengths, while Ba₂LaTaO₆ and PEA₂PbI₄ NCs have successfully extended operating wavelengths beyond 1,570 nm, enhancing their versatility in telecommunications and industrial laser applications. In this context, our work introduces BtzBiI₄ as a distinctive lead-free alternative, offering both environmental sustainability and excellent nonlinear optical response. Its demonstrated ability to support high-order harmonic modelocking at ultrahigh repetition rates distinguishes it from previously studied materials, underscoring its potential for demanding applications such as optical frequency comb generation and high-speed optical communication systems.

6 Results and discussion

In this study, we successfully synthesized the bismuthbased perovskite crystal BtzBiI₄ and fabricated a sandwichstructured BtzBiI₄-SA, which was subsequently applied to an EDFL. The saturable absorption properties of BtzBil₄-SA were characterized using the balanced twin-detector technique, yielding a MD of 8.51 %, a I_{sat} of 47.19 MW/cm², and a $T_{\rm ns}$ of 60.09 %. These results demonstrate its excellent saturable absorption performance. In an EDFL cavity with a total length of 22.11 m, fundamental mode-locking was achieved, producing pulses with a duration of 844 fs. By increasing the pump power and adjusting the polarization state, HML at orders of 28th, 41st, 55th, 65th, 70th, 76th, 92nd, 106th, 108th, 112nd, 114th, 122nd, 126th, 131th, and 142nd was observed, with the 142nd harmonic exhibiting a repetition rate as high as 1.3202 GHz. Additionally, bound-state soliton mode-locking was recorded at a central wavelength of 1,560.04 nm. The findings demonstrate that BtzBiI₄ possesses outstanding nonlinear optical properties, positioning it as an excellent candidate for use as a SA in EDFLs. In addition to its impressive performance, BtzBiI₄-SA exhibits remarkable environmental stability, cost efficiency, and a compact, alignment-free all-fiber design, highlighting its extensive potential across diverse applications. Particularly, the 1.3 GHz repetition rate pulses generated in this work fill a critical gap in the use of perovskite crystals as saturable absorbers in high repetition rate fiber laser systems. The laser's high stability and narrow pulse characteristics make it well-suited for a wide range of applications, including optical communications, optical frequency combs, optical imaging, lidar, industrial laser processing, and nonlinear optics. This study paves the way for the broader adoption of BtzBiI₄, a perovskite crystal, in ultrafast photonics, presenting promising avenues for future advancements in the field.

Research funding: This work was supported in part by the Natural Science Foundation of China under Grant 61705080. Author contributions: XD: writing, concept, execution. CL: data acquisition. ZD: data acquisition. YZ: execution. CZ: analysis, guidance. YW: data acquisition, guidance. PW: guidance, critical revision. All authors have accepted responsibility for the entire content of this manuscript and consented to its submission to the journal, reviewed all the results, and approved the final version of the manuscript. **Conflict of interest:** Authors state no conflicts of interest. Data availability: The datasets generated and/or analyzed during the current study are available from the corresponding author upon reasonable request.

References

[1] J. Kim and Y. Song, "Ultralow-noise mode-locked fiber lasers and frequency combs: principles, status, and applications," Adv. Opt. *Photonics*, vol. 8, no. 3, pp. 465 – 540, 2016.

- [2] S. A. Diddams, L. Hollberg, and V. Mbele, "Molecular fingerprinting with the resolved modes of a femtosecond laser frequency comb," Nature, vol. 445, no. 7128, pp. 627-630, 2007.
- [3] H. Kalaycıoğlu, P. Elahi, Ö. Akçaalan, and F. Ö. Ilday, "High-repetition-rate ultrafast fiber lasers for material processing," IEEE J. Sel. Top. Quantum Electron., vol. 24, no. 3,
- [4] L. J. Mortensen, et al., "Femtosecond laser bone ablation with a high repetition rate fiber laser source," Biomed. Opt. Express, vol. 6, no. 1, pp. 32-42, 2014.
- [5] M. Liu, R. Tang, A. P. Luo, W. C. Xu, and Z. C. Luo, "Graphene-decorated microfiber knot as a broadband resonator for ultrahigh-repetition-rate pulse fiber lasers," Photonics Res., vol. 6, no. 10, pp. C1 – C7, 2018.
- [6] W. Du, H. Xia, H. Li, C. Liu, P. Wang, and Y. Liu, "High-repetition-rate all-fiber femtosecond laser with an optical integrated component," Appl. Opt., vol. 56, no. 9, pp. 2504-2509, 2017.
- [7] X. M. Tan, et al., "Tunable and switchable dual-waveband ultrafast fiber laser with 100 GHz repetition-rate," Opt. Express, vol. 25, no. 14, pp. 16291-16299, 2017.
- [8] G. E. Villanueva, M. Ferri, and P. Perez-Millan, "Active and passive mode-locked fiber lasers for high-speed high-resolution photonic analog-to-digital conversion," IEEE J. Quantum Electron., vol. 48, no. 11, pp. 1443-1452, 2012.
- L. E. Nelson, D. J. Jones, K. Tamura, H. A. Haus, and E. P. Ippen, "Ultrashort-pulse fiber ring lasers," Appl. Phys. B Laser Opt., vol. 65, no. 2, 1997, https://doi.org/10.1007/s003400050273.
- D. Y. Tang, L. M. Zhao, B. Zhao, and A. Q. Liu, "Mechanism of [10] multisoliton formation and soliton energy quantization in passively mode-locked fiber lasers," Phys. Rev. A, vol. 72, no. 4, p. 043816, 2005.
- [11] D. D. Han, X. M. Liu, Y. D. Cui, G. X. Wang, C. Zeng, and L. Yun, "Simultaneous picosecond and femtosecond solitons delivered from a nanotube-mode-locked all-fiber laser," Opt. Lett., vol. 39, no. 6, pp. 1565-1568, 2014.
- [12] G. Sobon, J. Sotor, and K. M. Abramski, "Passive harmonic mode-locking in Er-doped fiber laser based on graphene saturable absorber with repetition rates scalable to 2.22 GHz," Appl. Phys. Lett., vol. 100, no. 16, p. 161109, 2012.
- [13] Z. C. Luo, et al., "2 GHz passively harmonic mode-locked fiber laser by a microfiber-based topological insulator saturable absorber," Opt. Lett., vol. 38, no. 24, pp. 5212-5215, 2013.
- [14] M. Liu, et al., "Microfiber-based few-layer MoS₂ saturable absorber for 2.5 GHz passively harmonic mode-locked fiber laser," Opt. Express, vol. 22, no. 19, pp. 22841-22846, 2014.
- [15] W. Huang, et al., "Highly stable MXene (V₂CT_x)-based harmonic pulse generation," Nanophotonics, vol. 9, no. 8, pp. 2577-2585, 2020
- [16] J. Lee, et al., "Harmonically mode-locked Er-doped fiber laser at 1.3 GHz using a V₂AIC MAX phase nanoparticle-based saturable absorber," Opt. Laser Technol., vol. 145, p. 107525, 2022.
- [17] L. Kong, et al., "Oxygen vacancy engineering of MOF-derived ZnO/Co₃O₄ nanocomposites for high harmonic mode-locking operation," J. Mater. Chem. C, vol. 10, no. 43, pp. 16564-16572,
- [18] M. Vali, D. Dideban, and N. Moezi, "Silicene field effect transistor with high on/off current ratio and good current saturation," J. Comput. Electron., vol. 15, pp. 138-143, 2016.

- [19] Z. Xu, et al., "Design of a tunable ultra-broadband terahertz absorber based on multiple layers of graphene ribbons," Nanoscale Res. Lett., vol. 13, no. 143, pp. 1-8, 2018.
- [20] K. Y. Lau and D. Hou, "Recent research and advances of material-based saturable absorber in mode-locked fiber laser," Opt Laser. Technol., vol. 137, p. 106826, 2021.
- [21] Q. H. Wang, K. Kalantar-Zadeh, A. Kis, J. N. Coleman, and M. S. Strano, "Electronics and optoelectronics of two-dimensional transition metal dichalcogenides," Nat. Nanotechnol., vol. 7, no. 11, pp. 699-712, 2012.
- [22] Z. Dou, Y. Song, J. Tian, J. Liu, Z. Yu, and X. Fang, "Mode-locked ytterbium-doped fiber laser based on topological insulator: Bi₂Se₃," Opt. Express, vol. 22, no. 20, pp. 24055 – 24061, 2014.
- [23] W. Li, et al., "212-kHz-linewidth, transform-limited pulses from a single-frequency Q-switched fiber laser based on a few-layer Bi₂Se₃ saturable absorber," *Photonics Res.*, vol. 6, no. 10, pp. C29 - C35, 2018.
- [24] K. Yan, et al., "Bi₂Te₃ based passively Q-switched fiber laser with cylindrical vector beam emission," Appl. Opt., vol. 55, no. 11, pp. 3026-3029, 2016.
- [25] K. Y. Lau, X. Liu, and J. Qiu, "MXene saturable absorbers in mode-locked fiber laser," Laser Photonics Rev., vol. 16, no. 9, p. 2100709, 2022.
- [26] L. Wang, et al., "Few-Layer mxene $Ti_3C_2T_x$ (T= F, O, or OH) for robust pulse generation in a compact Er-doped fiber laser," ChemNanoMat, vol. 5, no. 9, pp. 1233-1238, 2019.
- [27] B. Guo, Q. L. Xiao, S. H. Wang, and H. Zhang, "2D layered materials: synthesis, nonlinear optical properties, and device applications," Laser Photonics Rev., vol. 13, no. 12, p. 1800327, 2019.
- [28] Z. Hui, et al., "CoS nanosheets for generation of vector soliton and bound solitons in nonlinear optical fiber system," Opt. Laser Technol., vol. 160, p. 109026, 2023.
- [29] X. Du, et al., "Application of Pr-MOFs as saturable absorbers in ultrafast photonics," J. Mater. Chem. C, vol. 12, no. 15, pp. 5400-5410, 2024.
- [30] Y. Yang, et al., "Mo₄/3B₂T₂/Co₃O₄ vdW heterostructure as saturable absorber for ultrafast pulse generation," Opt. Laser Technol., vol. 180, p. 111599, 2025.
- [31] X. Du, P. Wang, S. Li, C. Liu, Z. Ding, and C. Zhu, "Study on pulse characteristics of high-repetition-rate harmonic mode-locked laser utilizing PbSnS₂ saturable absorber," *Infrared Phys. Technol.*, vol. 137, p. 105179, 2024.
- [32] Y. Y. Wang, et al., "In situ prepared ionic liquids containing moisture-resistant bismuth-based perovskite crystals enhance the photocatalytic water purification and H₂ production of MOF," Sep. Purif. Technol., vol. 360, p. 130998, 2024.
- [33] L. Zhang, et al., "Advances in the application of perovskite materials," Nano-Micro Lett., vol. 15, no. 1, p. 177, 2023.
- [34] B. Yang, et al., "Precise in-situ modulation of bandgap-controlled single-crystalline perovskite microlasers," J. Mater. Sci. Technol., vol. 214, pp. 27-36, 2025.
- [35] M. A. Green, A. Ho-Baillie, and H. J. Snaith, "The emergence of perovskite solar cells," Nat. Photonics, vol. 8, no. 7, pp. 506-514, 2014.
- [36] Y. Rong, et al., "Challenges for commercializing perovskite solar cells," Science, vol. 361, no. 6408, p. eaat8235, 2018.
- [37] Y. Xu, et al., "Recent progress of electrode materials for flexible perovskite solar cells," Nano-Micro Lett., vol. 14, no. 1, p. 117, 2022.

- [38] H. S. Jung, G. S. Han, N. G. Park, and M. J. Ko, "Flexible perovskite solar cells," Joule, vol. 3, no. 8, pp. 1850-1880, 2019.
- [39] A. Fakharuddin, et al., "Perovskite light-emitting diodes," Nat. Electron., vol. 5, no. 4, pp. 203-216, 2022.
- [40] X. Zhang, et al., "Perovskite random lasers on fiber facet," Nanophotonics, vol. 9, no. 4, pp. 935-941, 2020.
- [41] F. Wang, et al., "Recent progress on electrical and optical manipulations of perovskite photodetectors," Adv. Sci., vol. 8, no. 14, p. 2100569, 2021.
- [42] C. Li, Y. Ma, Y. Xiao, L. Shen, and L. Ding, "Advances in perovskite photodetectors," InfoMat, vol. 2, no. 6, pp. 1247-1256, 2020.
- [43] T. Lyu, P. Dorenbos, P. Xiong, and Z. Wei, "LiTaO₃: Bi³⁺, Tb³⁺, Ga³⁺, Ge⁴⁺: a smart perovskite with high charge carrier storage capacity for X-ray imaging, stress sensing, and non-real-time recording," Adv. Funct. Mater., vol. 32, no. 39, p. 2206024, 2022.
- [44] X. Xiang, H. Ouyang, J. Li, and Z. Fu, "Humidity-sensitive CsPbBr₃ perovskite based photoluminescent sensor for detecting water content in herbal medicines," Sensor. Actuator. B Chem., vol. 346, p. 130547, 2021.
- [45] M. Jung, S. G. Ji, G. Kim, and S. I. Seok, "Perovskite precursor solution chemistry: from fundamentals to photovoltaic applications," Chem. Soc. Rev., vol. 48, no. 7, pp. 2011-2038, 2019.
- [46] B. Shi, L. Duan, Y. Zhao, J. Luo, and X. Zhang, "Semitransparent perovskite solar cells: from materials and devices to applications," Adv. Mater., vol. 32, no. 3, p. 1806474, 2020.
- [47] M. V. Kovalenko, L. Protesescu, and M. I. Bodnarchuk, "Properties and potential optoelectronic applications of lead halide perovskite nanocrystals," Science, vol. 358, no. 6364, pp. 745-750, 2017.
- [48] C. Ma, H. Li, M. Chen, Y. Liu, K. Zhao, and S. Liu, "Water-resistant lead-free perovskitoid single crystal for efficient X-ray detection," Adv. Funct. Mater., vol. 32, no. 30, p. 2202160, 2022.
- [49] H. Yu, et al., "Broadband nonlinear optical response of lead telluride quantum dots for all-solid-state pulse lasers from visible to mid-infrared," Opt. Express, vol. 32, no. 26, pp. 46586 – 46598,
- [50] J. Zhu, et al., "MXene V₂CT_v nanosheet/bismuth quantum dot-based heterostructures for enhanced flexible photodetection and nonlinear photonics," ACS Appl. Nano Mater., vol. 6, no. 14, pp. 13629-13636, 2023.
- [51] T. Finke, J. Nürnberg, V. Sichkovskyi, M. Golling, U. Keller, and J. P. Reithmaier, "Temperature resistant fast In_xGa_{1-x}As/GaAs quantum dot saturable absorber for the epitaxial integration into semiconductor surface emitting lasers," Opt. Express, vol. 28, no. 14, pp. 20954-20966, 2020.
- [52] T. Du, et al., "NIR-activated multi-hit therapeutic Ag₂S quantum dot-based hydrogel for healing of bacteria-infected wounds," Acta Biomater., vol. 145, pp. 88-105, 2022.
- [53] Z. Chen, et al., "Light-quided genetic scissors based on phosphorene quantum dot," Laser Photonics Rev., vol. 18, no. 11, p. 2400777, 2024.
- [54] Z. Chen, et al., "Ultrasensitive DNA origami plasmon sensor for accurate detection in circulating tumor DNAs," Laser Photonics Rev., vol. 18, no. 10, p. 2400035, 2024.
- [55] Z. Chen, et al., "CRISPR-Cas13a-powered electrochemical biosensor for the detection of the L452R mutation in clinical samples of

- SARS-CoV-2 variants," J. Nanobiotechnol., vol. 21, no. 1, p. 141,
- [56] Y. Hu, et al., "Enhanced Q-switching performance of magnetite nanoparticle via compositional engineering with Ti₃C₂ MXene in the near infrared region," J. Mater. Sci. Technol., vol. 81, pp. 51-57,
- [57] J. Huang, N. Dong, N. Mcevoy, L. Wang, H. Wang, and J. Wang, "Exciton-like and mid-gap absorption dynamics of PtS in resonant and transparent regions," Laser Photonics Rev., vol. 16, no. 6, p. 2100654, 2022.
- [58] L. Kong, et al., "Enhanced nonlinear optical response and ultrafast carrier dynamics in amorphous Fe-doped ZIF-67," Mater. Chem. Front., vol. 8, no. 8, pp. 1971 – 1980, 2024. https://pubs.rsc.org/en/ content/articlelanding/2024/gm/d3gm01314f.
- [59] O. Zhao, H. Chu, Z. Pan, H. Pan, S. Zhao, and D. Li, "Surface oxygen vacancies in amorphous Fe₂O₃ tailored nonlinear optical properties for ultrafast photonics," J. Materiomics, vol. 11, no. 4, p. 100976, 2024.
- [60] N. Li, et al., "Highly stable pulsed fiber laser generation modulated by chromium iodide film," Nanophotonics, vol. 12, no. 23, pp. 4329-4337, 2023.
- [61] J. Wang, et al., "Wavelength and interval tunable second-order bound solitons in mode-locked fiber laser based on Lyot filter," Results Phys., vol. 58, p. 107479, 2024.
- [62] D. Zhang, C. Zhang, X. Li, and A. Qyyum, "Layered iron pyrite for ultrafast photonics application," Nanophotonics, vol. 9, no. 8, pp. 2515-2522, 2020.
- [63] Y. Zhou, Z. Hu, Y. Li, J. Xu, X. Tang, and Y. Tang, "CsPbBr₃ nanocrystal saturable absorber for mode-locking ytterbium fiber laser," Appl. Phys. Lett., vol. 108, no. 26, p. 261108, 2016.

- [64] P. Li, et al., "Two-dimensional CH₃NH₃PbI₃ perovskite nanosheets for ultrafast pulsed fiber lasers," ACS Appl. Mater. Interfaces, vol. 9, no. 14, pp. 12759 – 12765, 2017.
- [65] G. Jiang, et al., "Ultrafast pulse generation from erbiumdoped fiber laser modulated by hybrid organic-inorganic halide perovskites," Appl. Phys. Lett., vol. 110, no. 16, p. 161111,
- [66] X. Bao, et al., "Ytterbium-doped fiber laser passively mode locked by evanescent field interaction with CH₂NH₃SnI₃ perovskite saturable absorber," J. Phys. D: Appl. Phys., vol. 51, no. 37, p. 375106,
- [67] S. Hong, et al., "Mode-locking of all-fiber lasers operating at both anomalous and normal dispersion regimes in the C-and L-bands using thin film of 2D perovskite crystallites," Laser Photonics Rev., vol. 12, no. 11, p. 1800118, 2018.
- [68] S. Yang, J. Li, L. Li, L. Zhang, and X. Zhang, "Mode-locking operation of an Er-doped fiber laser with (PEA)₂(CsPbBr₃)_{n-1}PbBr₄ perovskite saturable absorbers," J. Mater. Chem. C, vol. 10, no. 19, pp. 7504-7510, 2022.
- [69] P. Guo, et al., "Nonlinear photonics device based on double perovskite oxide Ba₂LaTaO₆ for ultrafast laser generation," Opt. Laser Technol., vol. 155, p. 108334, 2022.
- [70] Y. He, et al., "Broadband nonlinear optical modulator with 2D organic-inorganic hybrid perovskite nanocrystals," IEEE J. Sel. Top. Quantum Electron., vol. 29, no. 6, pp. 1-8, 2023.

Supplementary Material: This article contains supplementary material (https://doi.org/10.1515/nanoph-2025-0087).